# Dynamic Magnetic Field Generation With High Accuracy Modeling Applied to Magnetic Robots

Qigao Fan[1], Pengsong Zhang[1], Juntian Qu[2], Wentao Huang[1], Xinyu Liu[3], and Linbo Xie[1]

[1]Department of Electrical Engineering and Automation, Jiangnan University, Wuxi 214122, China
[2]Department of Mechanical Engineering, Tsinghua University, Beijing 100084, China
[3]Department of Mechanical and Industrial Engineering, University of Toronto, Toronto, ON M5S 3G8, Canada

**Magnetic field driving technology is one of the research focuses in the field of micro/nanorobot motion control. In order to enhance the accuracy of magnetic field generation, a new drive circuit using the bipolar linear power amplifier, instead of the traditional switching elements, is designed for electromagnetic coil in this article. Meanwhile, an advanced control strategy is proposed to improve the dynamic and steady-state performance of magnetic field generation. The proposed approach mainly consists of the intelligent algorithm of neural network (NN) and proportional resonant differential feed-forward (PRDF) method. The NN algorithm is used to obtain the optimal parameters for the PRDF model. The feed-forward control is applied to eliminate the system disturbance caused by the coil temperature rise. Finally, comparative experiments with different control schemes are conducted for the combined coils of Maxwell and Helmholtz with multiple degrees of freedom. The experimental validations have revealed strong adaptability of the proposed scheme for different types of electromagnetic coils, as well as the satisfactory dynamic performance and steady-state precision.**

*Index Terms*— **Electromagnetic field control, magnetic micro/nanorobot, neural network (NN), proportional resonant differential (PRD).**

## I. Introduction

RECENT studies have shown that micro/nanorobots have extensive application prospects in biomedical research such as targeted drug delivery, hyperthermia, biopsy, heart stent implantation, minimally invasive surgery, and biological labeling [1]–[4]. Magnetic field driving technology has unique advantages [5], among various driving methods of microrobots, as it is considered harmless to organisms and has the ability to penetrate deep tissues. Currently, among the research areas in magnetic microrobots, the adopted forms of magnetic fields to drive microrobots mainly include gradient magnetic field, rotating magnetic field, and oscillating magnetic field [6]. In the mode of gradient magnetic field, the microrobots have a tendency to move along the gradient direction [7], [8], and the movement speed is related to the gradient magnitude [9]. The reason for utilizing the rotating magnetic fields for the actuation of magnetic microrobots is that the body of microrobots can rotate under the influence of a rotating magnetic field in a liquid environment and then generate the propulsion force to make microrobots flexible to move [10]. The microrobots' shapes under the rotating magnetic field mainly contain spiral structure type [11] and flagellum type [12]. Adopting the oscillating magnetic field method can make the microrobot capable of swinging the tail back and forth like a fish and generate forward propulsion force to making it move [13]. Among these driving methods, both the rotating magnetic field and the oscillating magnetic field are periodic magnetic

fields, and some operating frequencies can even reach up to 200 Hz [14]. Many different types of electromagnetic coils [6]–[16] have been developed by the research groups for different magnetic field types. Therefore, the exploration of high-precision dynamic magnetic field generation technology for different electromagnetic coils is very significant for the high-precision control of microrobots motion, which is also a hotspot.

In order to generate a high-precision dynamic magnetic field, the current of the coil should be precisely controlled. Generally, commercial digital controlled switching power supplies [17]–[21] are chosen, which can directly convert the digital signal setting into the coil's current output. Also, the power inverters [22]–[24] of the switching device are often selected to change the magnetic field by controlling the dynamic applied voltage on the coil. However, since the above-mentioned methods all use switching power devices as the circuit topology and pulsewidth modulation (PWM) technology as the current control method, current ripples are inevitably generated. As a result of the current ripples, magnetic field fluctuation occurs. These fluctuations limit the operating time of the coils and decrease the predictability of the field, which is an essential component for the generation of the field. Although the filter module can be added to the end of the power output, it can bring the phase lag of the magnetic field. In addition, various control methods, such as conventional proportional–integral (PI) control [24] and discrete-time optimal control [22], are studied to improve the quality of closed-loop magnetic field control devices. Since PI controllers are designed only by taking advantage of the output error information, PI control may not be the best control approach for many cases. Besides, since the potential PI gains are limited due to the presence of various types
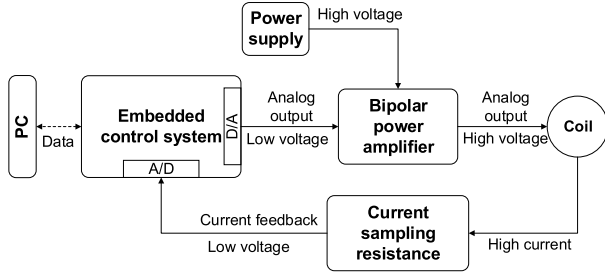
Fig. 1. Schematic representation of the electromagnetic coil system driven by a bipolar linear power amplifier.
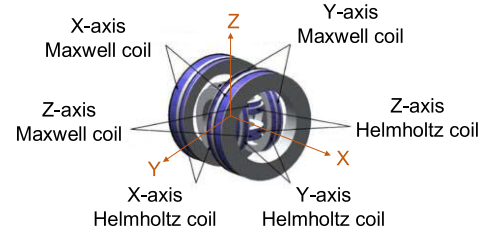


Fig. 2. Helmholtz and Maxwell coils.

TABLE I
PARAMETERS OF COMBINED COILS (THREE-AXIS HELMHOLTZ COILS AND THREE-AXIS MAXWELL COILS)

| Coil | Inductance (mH) | Resistance (Ω) |
|------|-----------------|----------------|
| Hx | 4.397 | 2.3 |
| Hy | 1.514 | 1.3 |
| Hz | 0.121 | 0.8 |
| Mx | 107.2 | 7.5 |
| My | 14.81 | 3.0 |
| Mz | 0.511 | 1.2 |

of noises, they cannot absolutely reduce the magnetic field tracking error by using only the PI control or advanced PI control [25]. Moreover, the phase–frequency characteristics of the electromagnetic coil system under variable frequency ac signal are not considered in the research of these literatures, and there may be a large phase error between the output magnetic field and the input command when the variable frequency field is needed.

The main contribution of this article is to propose a neural network adaptive quasi-proportional resonant differential feed-forward (NN-PRDF) control method based on bipolar linear power amplifier circuits for the electromagnetic coil system. Among them, the additional current ripple and noise are not introduced to the system because the PWM method is replaced by a power amplifier circuit to control the current; thereby, the control accuracy of the magnetic field is improved. Apart from the proportional resonant (PR) controller, differential and feed-forward modules are also added to improve the performance of the system. Furthermore, to make the controller have a good performance at different frequencies, the NN technology is applied to the electromagnetic coil system to optimize the parameters of the PRDF through a flexible design. By the proposed scheme, dynamic and high-precision magnetic field generation is realized. And the adaptability of electromagnetic coils with different parameters is improved.

The remaining part of this article is structured as follows: Section II introduces the self-customized electromagnetic coil system. Section III introduces the electromagnetic coil system model and the rotating magnetic field generation model. Section IV introduces the design of the NN-PRDF controller. Section V provides the experimental demonstration of the electromagnetic coil system. Finally, the implementation method is discussed and the conclusion is summarized in Section VI.

## II. SYSTEM OVERVIEW

The structure of an electromagnetic coil system utilized to drive microrobots is shown in Fig. 1, which consists of four major parts: the power supply for providing energy to the driving module of the electromagnetic coil system, electromagnetic coils for the generation of dynamic magnetic fields, a driving module for providing dynamic current in an electromagnetic coil, and a computer which coordinates with the driving module to optimize the closed-loop control system. In order to actuate various types of microrobots, it is necessary to configure electromagnetic coils with different

parameters to generate various forms of magnetic fields, such as gradient magnetic field, rotating magnetic field, and oscillating magnetic field. Therefore, the control scheme should be equipped with a simple process of parameter modification to adapt different electromagnetic coils quickly. In this article, the combination of Maxwell coils and Helmholtz coils is employed to illustrate the unique feature of the proposed control scheme.

### A. Combined Electromagnetic Coils

It is necessary to generate an independent controllable space magnetic field to realize the controllable movement of microrobots under the effect of the magnetic field. As shown in Fig. 2, the combined electromagnetic coil comprises a group of Helmholtz coils with three independent orthogonal directions and a group of three Maxwell coils with independent orthogonal directions. Their parameters are listed in Table I.

The Helmholtz coil produces a uniform magnetic field along its axial direction. As shown in the following formula, the magnetic field strength has a linear relationship with the current [26], where $\mu_0$, $N$, and $a$ are the vacuum magnetic permeability, turns of each coil, and radius of the coil, respectively:

$$B_{\mathrm{H}}(t) = \left(\frac{4}{5}\right)^{\frac{3}{2}} \frac{\mu_0 N I(t)}{a}. \tag{1}$$

The Maxwell coil produces a uniform gradient magnetic field along its axial direction [16]. From (2), the strength of the uniform magnetic field gradient is linear with the current, where $\mu_0$, $N$, and $a$ are the vacuum magnetic permeability, turns of each coil, and radius of the coil, respectively,

$$B'_{\mathrm{M}}(t) = g_{\mathrm{m}}(t) = \frac{16}{3}\left(\frac{3}{7}\right)^{\frac{5}{2}} \frac{\mu_0 N I(t)}{a^2}. \tag{2}$$

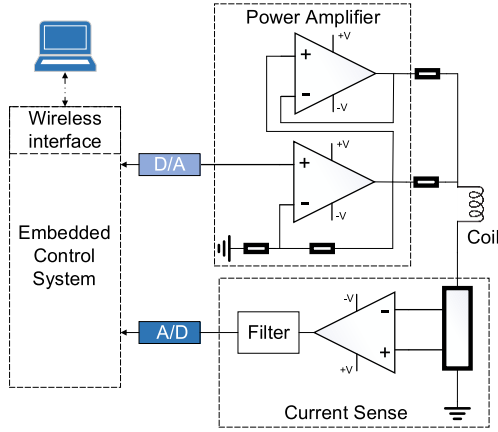The magnetic field strength and magnetic field gradient magnitude can be accurately detected by the current sensor

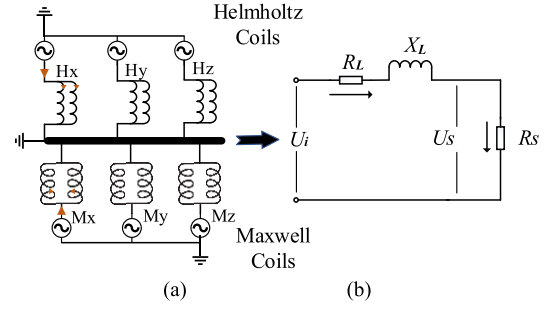Fig. 3. Schematic of the bipolar current source.



Fig. 4. (a) Model of combined electromagnetic coils. (b) Equivalent model of a single-axis electromagnetic coil.



Fig. 5. Rotational magnetic field diagram in spherical coordinates.

because of the relationship between the magnetic field and current in two types of coils. This will not degrade generality, because when the magnetic microrobot is working in its linear magnetization region, the linear relationship of the magnetic field and current is still established [27]; we take advantage of this feature in the following experiments.

### B. Driver Circuit Board for Driving the Combined Electro-magnetic Coils

The circuit board we developed is shown in Fig. 3, and it has an embedded control system based on the digital microcontroller unit (MCU). The control algorithm is executed by the MCU, and the computed control output in each control interval is converted to a low-voltage signal by the digital–analog conversion (DA) circuit (DAC8563; resolution: 16 bits; setting time: 10 $\mu$s) to control the high voltage exerted on the coils through a power amplifier circuit (PA07, $\pm$50 V, 10 A). The current flowing through the coils can be converted into a low-voltage signal by the sampling circuit (AD8429; input noise: 1 nV/$\sqrt{\text{Hz}}$; output noise: 45 nV/$\sqrt{\text{Hz}}$), and then converted into a digital signal by the analog–digital conversion (AD) circuit (ADS131A04, resolution up to 24 bits, data rates up to 128 kS/s) to the MCU. In addition, the communication interface circuit is used to exchange data between the driver board and PC. The input–output relationship of the power amplifier circuit is shown in the following formula:

$$V_{\text{out}} = \alpha V_{\text{in}}. \tag{3}$$

## III. SYSTEM MODEL

### A. Electromagnetic Coil System Model

Fig. 4(a) is a simplified schematic of the combined coils. Each axis coil can be regarded as a simple equivalent model, as shown in Fig. 4(b), where $R_{\text{L}}$ is the internal resistance of inductor, $X_{\text{L}}$ is the inductive reactance, and $R_{\text{s}}$ is the sampling resistance. The mutual inductance between the coils is not considered here because the coils are orthogonal and the mutual inductance has limited influence [22]. The transfer
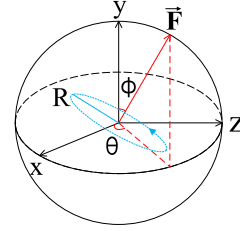
function is the following formula:

$$G(s) = \frac{R_{\text{s}}}{R_{\text{L}} + Ls}. \tag{4}$$

Ignoring the sampling resistance value, the voltage of the uniaxial coil is only related to resistance, inductance, and current (5). Therefore, the parameters of the electromagnetic coil can be easily measured based on the frequency characteristics of the inductance and resistance, as follows:

$$U = \sqrt{U_{\text{R}}^2 + U_{\text{L}}^2} = \sqrt{(IR)^2 + (IX_{\text{L}})^2} \tag{5}$$

$$Z = \sqrt{R^2 + X_{\text{L}}^2} \tag{6}$$

$$X_{\text{L}} = 2\pi f L. \tag{7}$$

Set $f = 0$, and measure the internal resistance $R$ as follows:

$$R = U/I. \tag{8}$$

The following measurement formula of $L$ can be obtained by combining (5)–(8)

$$L = \frac{\sqrt{U^2/(I^2 - R^2)}}{2\pi f}. \tag{9}$$

### B. Model Design of the Space Rotating Magnetic Field

A space rotating magnetic field can be generated in the working space by using the three-axis Helmholtz coils. As shown in Fig. 5, a spherical coordinate system is used to express the axial direction of the rotating magnetic field. Take the movement of a rotary-propelling microrobot as an example, $\vec{F} = (\vec{F}_x, \vec{F}_y, \vec{F}_z) = (F, \phi, \theta)$, where $\vec{F}$ is the axial vector of the rotating magnetic field, $\phi$ and $\theta$ are the azimuth angle and elevation angle, respectively, and $F$ is the magnitude of force.
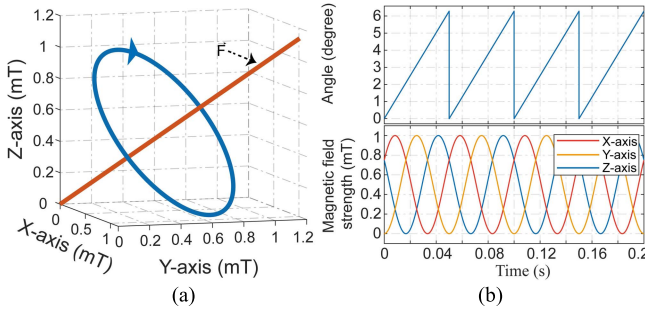
Fig. 6. (a) Schematic of the space magnetic field rotating at 20 Hz along the normal vector (0,0,1). (b) Waveform diagram of the relationship between the rotation angle along the axis and the magnetic field generated by the coil on each axis.



Fig. 7. (a) Comparison between the PI method and PRD method with Bode diagram. (b) Sine wave tracking performance.

In order to generate a spatial rotating magnetic field around $\vec{F}$, convert $\vec{F}$ into a rotation axis vector $\overrightarrow{(v_x, v_y, v_z)}$. Randomly select an initial position $(x, y, z)$ which is perpendicular to $\vec{F}$ and the distance to the rotation axis is $R$. Then, take the initial position $(x, y, z)$ as the starting point to rotate around the rotation axis vector $\overrightarrow{(v_x, v_y, v_z)}$ to get a series of $(x', y', z')$. Assuming that the rotated angle is $\theta$, the rotated magnetic field can be expressed by the following equations, and the simulation of the rotating magnetic field is shown in Fig. 6:

$$
\begin{aligned}
x' = {} & (v_x \cdot v_x \cdot (1 - \cos\theta) + \cos\theta) \cdot x \\
& + (v_x \cdot v_y \cdot (1 - \cos\theta) - v_z \cdot \sin\theta) \cdot y \\
& + (v_x \cdot v_z \cdot (1 - \cos\theta) + v_y \cdot \sin\theta) \cdot z \quad (10)
\end{aligned}
$$

$$
\begin{aligned}
y' = {} & (v_x \cdot v_y \cdot (1 - \cos\theta) + v_z \cdot \sin\theta) \cdot x \\
& + (v_y \cdot v_y \cdot (1 - \cos\theta) + \cos\theta) \cdot y \\
& + (v_y \cdot v_z \cdot (1 - \cos\theta) - v_x \cdot \sin\theta) \cdot z \quad (11)
\end{aligned}
$$

$$
\begin{aligned}
z' = {} & (v_x \cdot v_z \cdot (1 - \cos\theta) - v_y \cdot \sin\theta) \cdot x \\
& + (v_y \cdot v_z \cdot (1 - \cos\theta) + v_x \cdot \sin\theta) \cdot y \\
& + (v_z \cdot v_z \cdot (1 - \cos\theta) + \cos\theta) \cdot z \quad (12)
\end{aligned}
$$

$$
\theta = 2\pi \cdot \int t \, dt. \quad (13)
$$

## IV. DESIGN OF THE NN-PRDF MAGNETIC FIELD CONTROLLER

The conventional PI controller may not be able to adapt well and may cause instability of the system when driving different electromagnetic coils or the load may change. Moreover, the PI control method is limited in steady-state margin and phase error [28] when the electromagnetic coils system needs to generate a rotating magnetic field or an oscillating magnetic field. In this section, a control scheme is proposed, including the design of the PRDF controller, as well as its optimization based on NN and loss function.

### A. PRDF Magnetic Field Controller

The proposed PRDF controller is improved based on PR technology [29], and the stability of the system can be secured as it can eliminate harmonics at the resonance frequency. The resonance frequency $\omega_0$ is set as the frequency of the
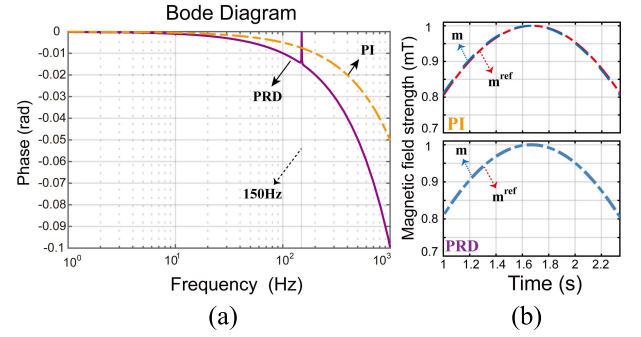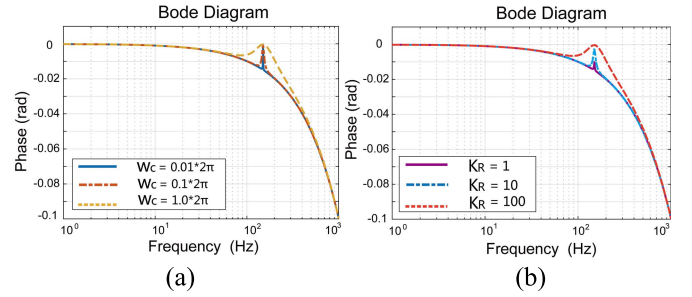


Fig. 8. Phase–frequency characteristics of PRD controller. (a) Keep $K_R$ unchanged, change $\omega_c$. (b) Keep $\omega_c$ unchanged, change $K_R$.

reference magnetic field to achieve zero error for the control of periodic magnetic field, and we added a differential block on the basis of the PR controller to optimize the control performance of the non-periodic magnetic field. The PRD controller can be expressed by the following transfer function:

$$
G(s) = K_p + \frac{2 K_R \omega_c s}{s^2 + 2\omega_c s + \omega_0^2} + K_d s. \quad (14)
$$

Here, $K_p$ is the proportional coefficient, $K_R$ is the gain coefficient of the resonance terms, $\omega_0$ is the resonance frequency, $\omega_c$ is the cutoff frequency, and $K_d$ is the differential coefficient. As the PR controller's gain is very small at the non-fundamental frequency, it cannot track the waveform effectively when the system is affected by frequency offset that is induced by analog system components or the digital system. However, the $\omega_c$ coefficient can help the system achieve zero steady-state error and make the system achieve good steady-state margin and transient performance as it can increase the gain of the fundamental frequency. The Bode plots and sine wave tracking waveforms of PI and PRD are shown in Fig. 7, and it can be seen that the PRD method has completely compensated the phase error at the resonance frequency.

Proportional control is used to improve the system's response speed and the differential control can reduce overshoot and restrain disorder. What is more, the PRDF controller also has two important parameters, $K_R$ and $\omega_c$. Fig. 8 shows the influence of different $K_R$ and $\omega_c$ values of the PRD controller on the frequency characteristics of the electromagnetic coil.

However, it is impossible to eliminate the magnetic field error in the variable frequency domain by using the PRD
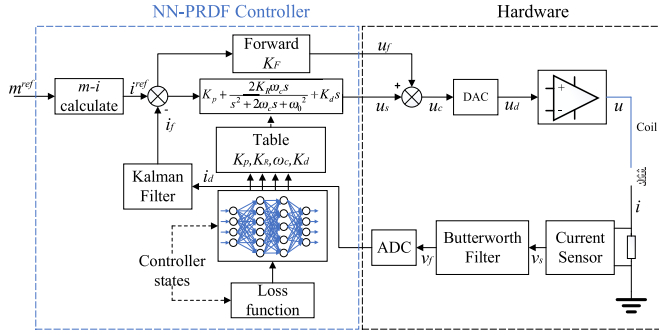
Fig. 9. Block diagram of the control loop of the NN-PRDF magnetic field controller.



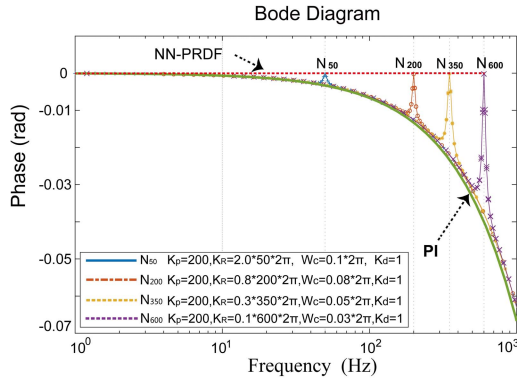Fig. 11. Two-hidden-layer backpropagation network structure.



Fig. 10. Bode diagram comparison between PI and PRDF method.

control technology alone. Therefore, as shown in Fig. 9, an adaptive current controller is designed by using an offline lookup table to store the parameters of the PRD controller at each different resonant frequency. The input of the lookup table is $\omega_0$, and the outputs are $K_P$, $K_R$, $\omega_c$, and $K_d$. In addition, a feed-forward control module is added to the magnetic field controller to estimate the reactance of the electromagnetic coil. The gain of this module used to enhance the PRD controller is calculated as follows:

$$K_F = \frac{1}{n} \sum_{j=1}^{n} \frac{v}{i} \tag{15}$$

where $n = 50$ represents that the initial sampling time is 50.

The PRDF controller trained by NN can improve its zero steady-state error tracking performance for sinusoidal signals at frequencies of 1–600 Hz. Fig. 10 shows the phase–frequency characteristics of the magnetic field at four different frequencies (50, 200, 350, and 600 Hz). The red dashed line is obtained by using 600 samples at 600 frequencies; this is the phase–frequency characteristics of the NN-PRDF controller. The phase error of the PI controller can be seen clearly in the Bode diagram, while the phase error of the NN-PRDF is near zero.

### B. Design of the NN

However, the manual selection of parameters from the Bode diagram of the PRDF controller is not a good choice, as it
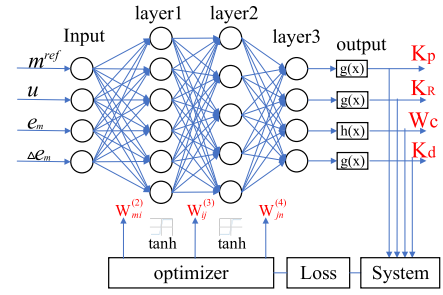
cannot perfectly reflect the actual electromagnetic coils model, especially when there is a change of electromagnetic coil parameters. Thus, the parameters should be corrected to obtain the smallest error of phase. That is why we propose the NN technique [30], which uses the online backpropagation of the gradient descent update method to calibrate the PRDF parameters. Discretization of the PRD controller can be expressed as follows:

$$u(n) = b_0 e(n) + b_1 e(n-1) + b_2 e(n-2)$$
$$+ b_3(e(n) - e(n-1)) - a_1 u(n-1) - a_2 u(n-2) \tag{16}$$

where $u(n)$ is the output of the PRD controller, $e(n) = m^{\text{ref}}(n) - m(n)$ is the magnetic field error, and

$$b_0 = \frac{(4 + 4T_s w_c + w_0^2 T_s^2) K_P + 4K_R T_s w_c}{4 + 4T_s w_c + w_0^2 T_s^2}$$

$$b_1 = \frac{(2w_0^2 T_s^2 - 8) K_P}{4 + 4T_s w_c + w_0^2 T_s^2}$$

$$b_2 = \frac{(4 + 4T_s w_c + w_0^2 T_s^2) K_P - 4K_R T_s w_c}{4 + 4T_s w_c + w_0^2 T_s^2}$$

$$b_3 = \frac{(4 + 4T_s w_c + w_0^2 T_s^2) K_d}{4 + 4T_s w_c + w_0^2 T_s^2}$$

$$a_1 = \frac{2w_0^2 T_s^2 - 8}{4 + 4T_s w_c + w_0^2 T_s^2}, \quad a_2 = \frac{4 - 4T_s w_c + w_0^2 T_s^2}{4 + 4T_s w_c + w_0^2 T_s^2}.$$

As shown in Fig. 11, an NN with two hidden layers is designed, and the first hidden layer has six neuron elements and the second hidden layer has five neuron elements. In addition, the parameters of the output layer are $K_P$, $K_R$, $\omega_c$, and $K_d$. The online backpropagation algorithm is applied for adjusting the weights of NN to reduce the tracking error of the magnetic field strength.

In order to achieve the new tuning parameters in the output of the NN, the input for the input layer is given as follows:

$$O_m^{(1)} = x_m \quad (m = 1, 2, 3, 4) \tag{17}$$

where $x = [m^{\text{ref}}, u, e_m, \Delta e_m]^{\text{T}}$.

The input and output of the first hidden layer are

$$\text{net}_i^{(2)}(k) = \sum_{m=1}^{4} w_{mi}^{(2)} x_m \tag{18}$$

$$O_i^{(2)}(k) = f\left(\text{net}_i^{(2)}(k)\right) \quad (i = 1, 2, 3, 4, 5). \tag{19}$$

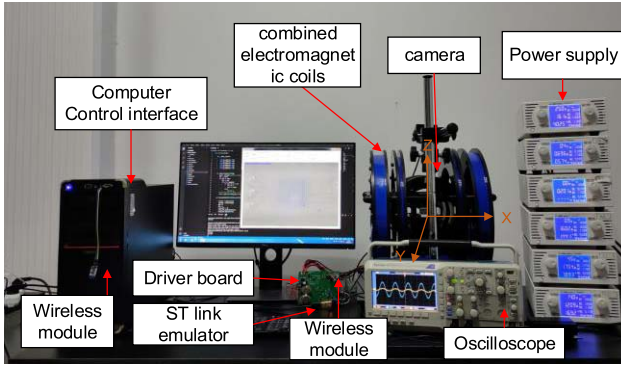IEEE TRANSACTIONS ON MAGNETICS, VOL. 57, NO. 7, JULY 2021
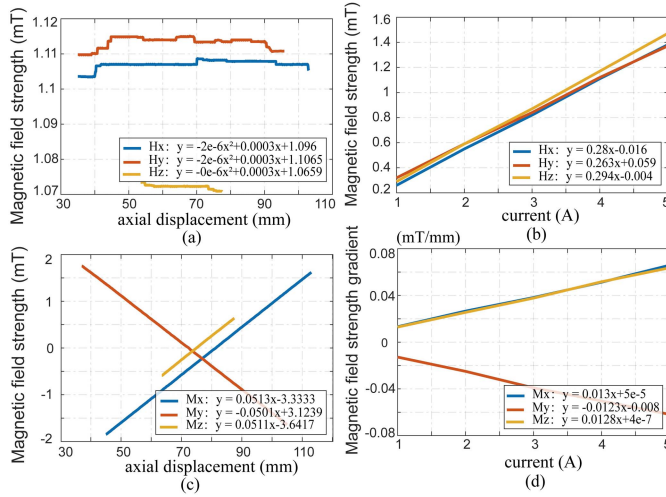


Fig. 12.   Experimental system.



Fig. 13.   Curve fitting. (a) Magnetic field strength and displacement curve of Helmholtz coils. (b) Magnetic field strength and current curve of Helmholtz coils. (c) Magnetic field gradient magnitude and displacement curve of Maxwell coils. (d) Magnetic field gradient magnitude and current curve of Maxwell coils.
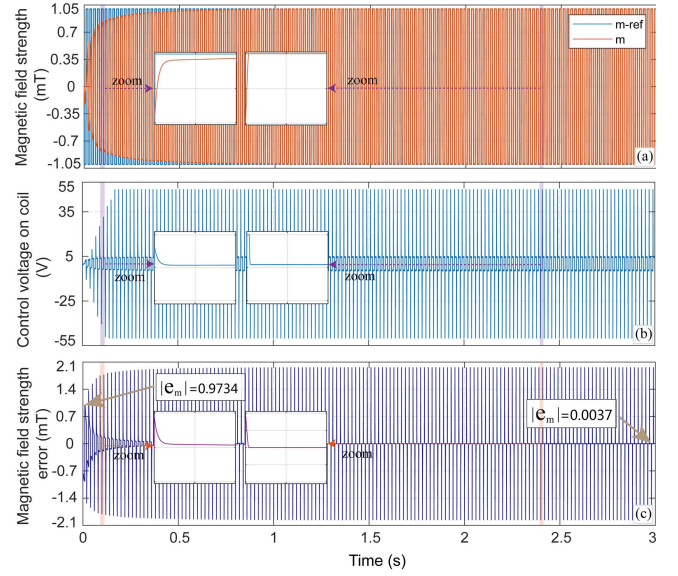


Fig. 14.   NN Calibration process for step response. (a) Magnetic field strength. (b) Control voltage on coil. (c) Magnetic field strength control error.
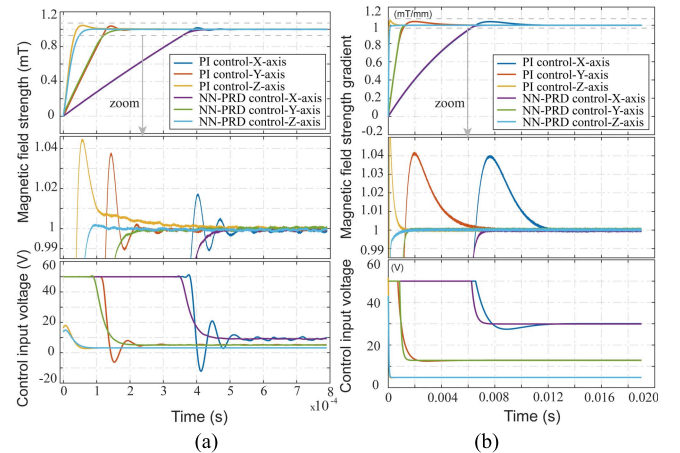


Fig. 15.   PI and NN-PRDF experimental results. (a) Helmholtz coils. (b) Maxwell coils.

The input and output of the second hidden layer are

$$\mathrm{net}_j^{(3)}(k) = \sum_{i=1}^{5} w_{ij}^{(3)}(k) O_j^{(2)}(k) \qquad (20)$$

$$O_j^{(3)}(k) = f\left(\mathrm{net}_j^{(3)}(k)\right) \quad (j = 1, 2, 3, 4, 5). \qquad (21)$$

For the output layer, the input and output are

$$\mathrm{net}_n^{(4)}(k) = \sum_{j=1}^{5} w_{jn}^{(4)}(k) O_n^{(2)}(k) \qquad (22)$$

$$O_n^{(4)}(k) = g\left(\mathrm{net}_n^{(4)}(k)\right) \quad (n = 1, 2, 3, 4) \qquad (23)$$

where $O^{(4)} = [K_P, K_R, W_c, K_d]^T$ is the final output of the network, $w_{mi}^{(2)}$, $w_{ij}^{(3)}$, and $w_{jn}^{(4)}$ are the weight coefficients of the hidden layer and the output layer, respectively. The upper corner marks (1), (2), (3), (4) indicate input layer, hidden layer 1, hidden layer 2, and output layer, respectively. The activation function used in the hidden layer is a tanh function with positive and negative symmetry $f(x) = ((e^x - e^{-x})/(e^x + e^{-x}))$. The output layer uses a non-negative sigmoid function $h(x) = (1/(1 + e^{-x}))$ and a soft-plus function $g(x) = \log(1 + e^x)$.

## C. Design of Loss Function

In order to make NN-PRDF have a faster rate of convergence, some common indexes in the control system are extracted to guide the design of loss function. The step response is used as excitation for the non-periodic magnetic field; therefore, we select rise time $t_r$, peak time $t_p$, setting time $t_s$, overshot $\sigma\%$ (25), and MSE (26) for tracking to guide the generation of loss function. However, for the periodic magnetic field, only MSE is used as the control system evaluation index. In order to collect and extract the control system index information of the step response, the NN update period time $T_n$ is set to be greater than the control period time $T_s$

$$\mathrm{Loss} = \alpha \frac{t_r}{T_n} + \beta \frac{t_p}{T_n} + \gamma \frac{t_s}{T_n} + \delta\sigma\% + \varepsilon\mathrm{MSE} \qquad (24)$$

$$\sigma\% = \frac{c(t_p) - c(\infty)}{c(\infty)} \times 100\% \qquad (25)$$

Authorized licensed use limited to: The University of Toronto. Downloaded on December 30,2021 at 19:40:54 UTC from IEEE Xplore. Restrictions apply.
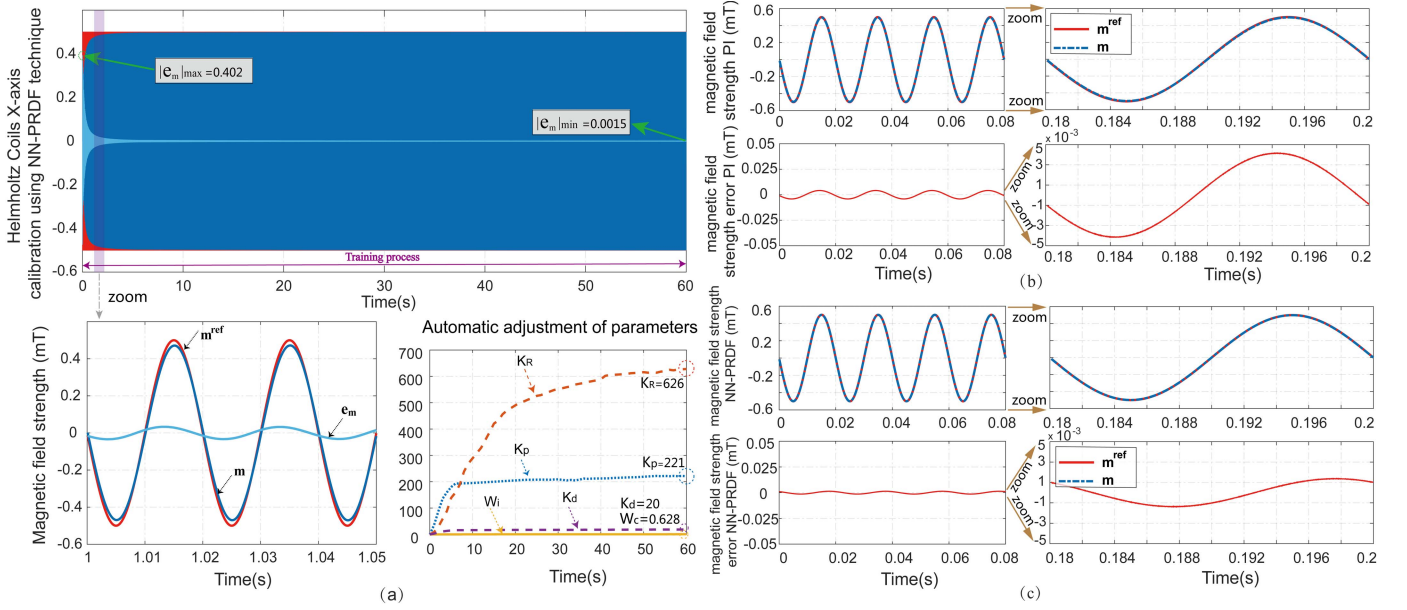
Fig. 16. (a) Controller regulation process by NN at 50 Hz. (b) Magnetic field tracking performance of the conventional PI controller. (c) Magnetic field tracking performance of the NN-PRDF controller.

$$\text{MSE} = \frac{1}{N} \sum_{n=1}^{N} \left( m_n^{\text{ref}} - m_n \right)^2 \qquad (26)$$

where $\alpha$, $\beta$, $\gamma$, $\delta$, and $\varepsilon$ are the coefficients of rise time, peak time, setting time, overshoot, and trajectory MSE, respectively. It is necessary to tune these parameters for different magnetic field forms and control system performance index. For the periodic magnetic field, only the tracking error is considered, so the coefficients are set as $[\alpha, \beta, \gamma, \delta, \varepsilon] = [0.0, 0.0, 0.0, 0.0, 1.0]$. Considering its performance index of step response for the non-periodic magnetic field, the coefficients are set as $[\alpha, \beta, \gamma, \delta, \varepsilon] = [0.1, 0.1, 0.1, 0.1, 0.6]$.

Taking $\eta$ as the learning rate and $\lambda$ as the inertia coefficient, these coefficients directly affect the convergence speed of the NN

$$\Delta w_{jn}^{(4)}(k) = \eta \frac{\partial \text{Loss}(k)}{\partial w_{jn}^{(4)}(k)} + \lambda \Delta w_{jn}^{(4)}(k-1) \qquad (27)$$

$$\frac{\partial \text{Loss}(k)}{\partial w_{jn}^{(4)}(k)} = \frac{\partial \text{Loss}(k)}{\partial y(k)} \cdot \frac{\partial y(k)}{\partial u(k)} \cdot \frac{\partial u(k)}{\partial O_n^{(4)}(k)}$$
$$\cdot \frac{\partial O_n^{(4)}(k)}{\partial \text{net}_n^{(4)}(k)} \cdot \frac{\partial \text{net}_n^{(4)}(k)}{\partial w_{jn}^{(4)}(k)}. \qquad (28)$$

Replacing $(\partial y(k)/\partial u(k))$ with $\text{sgn}(\partial y(k)/\partial u(k))$, the final error is compensated by the learning rate $\eta$, which can be written as follows:

$$\Delta w_{jn}^{(4)}(k) = \lambda \Delta w_{jn}^{(4)}(k-1) + \eta \delta_n^{(4)} O_j^{(3)}(k) \qquad (29)$$

$$\delta_n^{(4)} = -\frac{\partial \text{Loss}(k)}{\partial \text{net}_n^{(4)}(k)} = e(k) \cdot \text{sgn}\left( \frac{\partial y(k)}{\partial u(k)} \right)$$
$$\cdot \frac{\partial u(k)}{\partial O_n^{(4)}(k)} \cdot g'\left( \text{net}_n^{(4)}(k) \right). \qquad (30)$$

Using the similar calculation

$$\Delta w_{ij}^{(3)}(k) = \lambda \Delta w_{ij}^{(3)}(k-1) + \eta \delta_i^{(3)} O_j^{(2)}(k) \qquad (31)$$

$$\delta_j^{(3)} = -\frac{\partial \text{Loss}(k)}{\partial \text{net}_j^{(3)}(k)} = f'\left( \text{net}_j^{(3)}(k) \right) \cdot \sum_{j=1}^{5} w_{jn}^{(4)}(k) \cdot \delta_i^{(4)} \qquad (32)$$

$$\Delta w_{mi}^{(2)}(k) = \lambda \Delta w_{mi}^{(2)}(k-1) + \eta \delta_m^{(2)} O_i^{(1)}(k) \qquad (33)$$

$$\delta_i^{(2)} = -\frac{\partial \text{Loss}(k)}{\partial \text{net}_i^{(2)}(k)} = f'\left( \text{net}_i^{(2)}(k) \right) \cdot \sum_{i=1}^{5} w_{ij}^{(3)}(k) \cdot \delta_i^{(3)}. \qquad (34)$$

As the weights are updated according to (29), (31), and (33), the control error will be reduced accordingly.

## V. EXPERIMENT AND ANALYSIS

### A. System Configuration

In order to validate the NN-PRDF control method, the experimental system setup (shown in Fig. 12) is utilized. The driver board is designed by the circuit design tool (ALTIUM DESIGNER 20, Altium Inc., Australia). It is necessary to implement a short sampling time to ensure the performance of the controller. Thus, the MCU (STM32-H743VIT6, 480 MHz, STMicroelectronics Inc., Switzerland) is used to apply the proposed algorithms (sampling time: 25 $\mu$s). The control algorithm on the embedded system (control frequency: 40 kHz) is coded by the C programming language and commanded by a PC using the ST-Link emulator. The NN is implemented based on the deep learning framework (PaddlePaddle, Baidu Inc., China) and deployed on a desktop computer (Intel Core i5-6500 CPU, 8 GB RAM, 3.2 GHz). Besides, PI controller is also implemented for comparison. The main contents of the experiment are explained in the subsequent subsections.

## B. Experiment on the Relationship Between the Magnetic Field and the Current of Combined Electromagnetic Coils

The uniform magnetic field and gradient magnetic field are generated by Helmholtz coils and Maxwell coils, respectively, and both of them are proportional to the current. Fig. 13(a) shows the magnetic field strength and displacement curve of Helmholtz coils; Fig. 13(b) shows the magnetic field strength and current curve of Helmholtz coils; Fig. 13(c) shows the magnetic field gradient magnitude and displacement curve of Maxwell coils; and Fig. 13(d) shows the magnetic field gradient magnitude and current curve of Maxwell coils. Formulas (1) and (2) can be verified by the curve fitting formula as shown in Fig. 13. By the curve fitting formula, the magnetic field can be obtained easily.

## C. Calibration Process and Experimental Results for Step Response

In order to obtain the NN-PRDF optimal parameters of step response, we selected the low-frequency square wave of 50 Hz to equivalent the step response. In each cycle of the square wave, 200 sets of sample data are collected at 100 $\mu$s intervals to calculate the loss value, and in the subsequent cycle, the new controller parameters are calculated by the updated NN model. In addition, the learning rate $\eta$ and the inertia term $\lambda$ are assumed to be $\eta = 0.01$ and $\lambda = 0.1$. Fig. 14(a) shows the training process of the $x$-axis of the Helmholtz coils in the combined coils. Due to the online backpropagation algorithm, the steady-state error of each cycle gradually decreases during the training process. Finally, the lowest magnetic field error is reached, and the system has no overshoot. As shown in Fig. 14(c), the steady-state magnetic field strength error has been reduced from 0.9734 to 0.0037 (mT).

We carried out the step response training process for each coil in the combined coils to obtain the optimal control parameters. The results of the step response for combined coils with the NN-PRDF control scheme and the PI controller are shown in Fig. 15. It can be seen that the overshoot of the Helmholtz coils' $z$-axis is reduced from 4.6% to 0.35% (92.3% improvement) and the setting time is reduced from 0.3 to 0.1 ms (67% improvement, which means the control frequency of the $z$-axis coil can reach 10 kHz), and the maximum setting time of the Maxwell coils is reduced from 12 to 6.9 ms (42% improvement, which means the dynamic tracking of magnetic fields with frequencies can reach 140 Hz). The analyses of each coil's experimental results are recorded and presented in Table II. The convergence speed shows that the electromagnetic system with NN-PRDF control can generate a high-precision magnetic field with higher frequency.

## D. Calibration Process and Experimental Results for the Space Rotating Magnetic Field

The working frequency range of the space rotating magnetic field generated by Helmholtz coils is from 1 to 600 Hz in the experiment. The 50 sets of sample data are collected to calculate the MSE loss value at each cycle for accelerating the convergence speed of the NN model and obtain the optimal

### TABLE II
### CONTROL PERFORMANCE COMPARISONS OF THE NN-PRDF CONTROL WITH CONVENTIONAL CONTROL METHODS

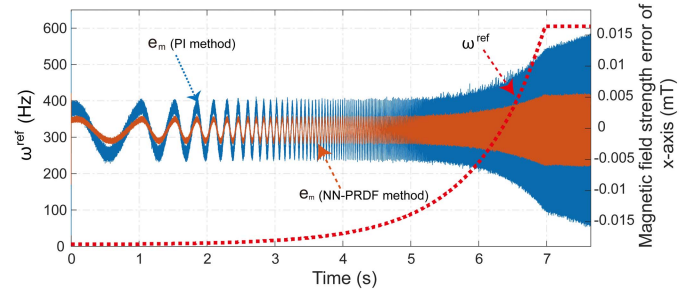| Control methods | | Hx | Hy | Hz | Mx | My | Mz |
|---|---|---|---|---|---|---|---|
| Pi | Setting time (ms) | 0.6 | 0.4 | 0.3 | 12.0 | 6.3 | 1.2 |
| | Overshoot (%) | 1.7 | 3.8 | 4.6 | 4.0 | 4.2 | 5.1 |
| NN-PRDF | Setting time (ms) | 0.5 | 0.2 | 0.1 | 6.9 | 2.1 | 0.7 |
| | Overshoot (%) | 0.11 | 0.12 | 0.35 | 0.12 | 0.11 | 0.12 |



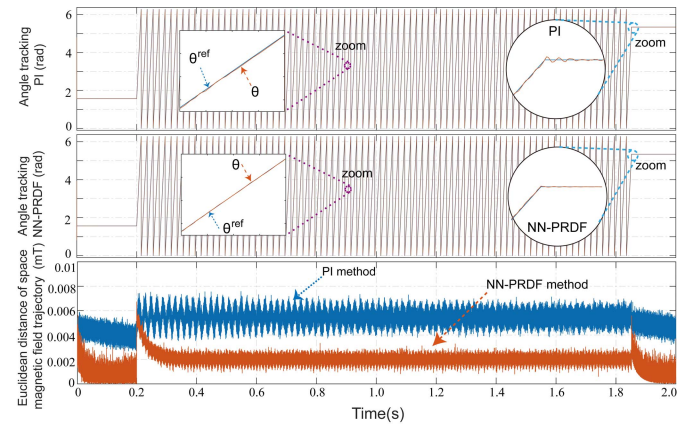Fig. 17. Dynamic speed regulation of space rotating magnetic field of NN-PRDF controller.



Fig. 18. Trajectory and angle tracking performance of space rotating magnetic field at 50 Hz.

controller parameters. In addition, the learning rate $\eta$ and the inertia term $\lambda$ are assumed to be $\eta = 0.025$ and $\lambda = 0.15$. Taking the $x$-axis of Helmholtz coils, for example, the training process at 50 Hz is shown in Fig. 16. It can be seen from the results that the traditional PI leads to a large magnetic field error, which is more than double the NN-PRDF method.

Then, a sweep frequency test is carried out to test the continuous impact of the NN-PRDF method. The reference speed and magnetic field error of the frequency sweep test are shown in Fig. 17. The space rotating magnetic field frequency generated by three-axis Helmholtz coils runs from 1 to 600 Hz, and the magnetic field strength error of the two methods are shown in Fig. 17. It is easily seen that the magnetic field strength error of $x$-axis is increased by 1.6 times (from 0.003 to 0.005), which is less than three times (from
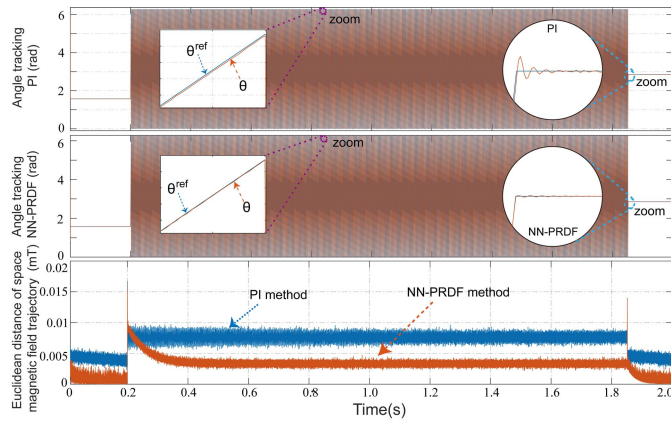
Fig. 19. Trajectory and angle tracking performance of space rotating magnetic field at 350 Hz.
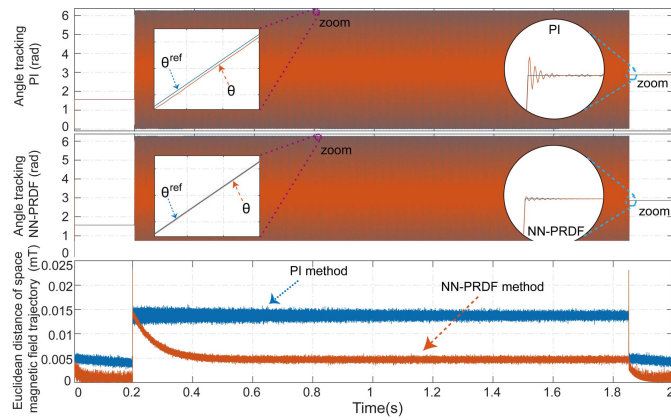


Fig. 20. Trajectory and angle tracking performance of space rotating magnetic field at 600 Hz.

TABLE III
COMPARISON OF THE RMSE AND MEAN $\theta$ ERROR BETWEEN THE PI METHOD AND THE NN-PRDF METHOD

| Control method | | 50 Hz | 350 Hz | 600 Hz |
|---|---|---|---|---|
| PI | RMSE | 0.008 | 0.022 | 0.039 |
| | Mean $\theta_e$ (°) | 0.181 | 1.261 | 2.591 |
| NN-PRDF | RMSE | 0.002 | 0.004 | 0.005 |
| | Mean $\theta_e$ (°) | 0.036 | 0.151 | 0.539 |

0.005 to 0.015) of the PI method. Therefore, we concluded that the NN-PRDF method has a smaller magnetic field strength error than PI method, and the method has achieved better magnetic field tracking performance and stability. This is a novel improvement that is easy to apply to the electromagnetic coils system.

Moreover, the angle tracking experiments of the space rotating magnetic field are shown in Figs. 18–20. The system is tested at a speed of 50, 350, and 600 Hz. We compared the conventional PI method with the NN-PRDF method. As can be seen, the conventional PI method has obvious anger phase error and brake fluctuation. When the NN-PRDF method is applied, the angle phase error, the fluctuation of the rotating brake, and the Euclidean distance between the real trajectory and the given trajectory of space magnetic field are all reduced.

Compared with the conventional method, it is obvious that this method has good stability and high accuracy. Specifically, the root mean square error (RMSE) and the mean angle tracking error of these methods are compared in Table III.

## VI. CONCLUSION

In order to guarantee the accuracy and dynamic performance of the electromagnetic coil system, a new adaptive control scheme based on the NN calibration technique and the proportional resonance control algorithm is proposed. The control system can automatically optimize the controller parameters via connecting the electromagnetic coil without the need of manual adjustment, facilitating its high adaptivity with different types of electromagnetic coils. In addition, the power amplifier used in the hardware owns excellent features of linear voltage amplification and high bandwidth, avoiding additional noise. To demonstrate the effectiveness of the proposed controller, the unit step response of Helmholtz coil and Maxwell coil and the space rotating magnetic field tracking performance of Helmholtz coil are validated, which show that the control frequencies of Maxwell coil and Helmholtz coil can reach 140 and 600 Hz, respectively, the maximum overshoot of unit step response is only 0.35%, and the average phase error in the angle tracking of the space rotating magnetic field does not exceed 0.6° in the frequency band (1–600 Hz). Experimental results indicate the proposed control scheme can significantly improve the dynamic performances of the control system, compensating the phase lag of the spatial rotating magnetic field and reducing the ripple.

## REFERENCES

[1] X. Yan *et al.*, "Multifunctional biohybrid magnetite microrobots for imaging-guided therapy," *Sci. Robot.*, vol. 2, no. 12, Nov. 2017, Art. no. eaaq1155.
[2] M. Sitti *et al.*, "Biomedical applications of untethered mobile milli/microrobots," *Proc. IEEE*, vol. 103, no. 2, pp. 205–224, Feb. 2015.
[3] J. Li, B. E.-F. de Ávila, W. Gao, L. Zhang, and J. Wang, "Micro/nanorobots for biomedicine: Delivery, surgery, sensing, and detoxification," *Sci. Robot.*, vol. 2, no. 4, Mar. 2017, Art. no. eaam6431.
[4] L. Yang, Y. Zhang, Q. Wang, K.-F. Chan, and L. Zhang, "Automated control of magnetic spore-based microrobot using fluorescence imaging for targeted delivery with cellular resolution," *IEEE Trans. Autom. Sci. Eng.*, vol. 17, no. 1, pp. 490–501, Jan. 2020.
[5] T. Xu, W. Gao, L.-P. Xu, X. Zhang, and S. Wang, "Fuel-free synthetic micro-/nanomachines," *Adv. Mater.*, vol. 29, no. 9, Mar. 2017, Art. no. 1603250.
[6] T. Xu, J. Yu, X. Yan, H. Choi, and L. Zhang, "Magnetic actuation based motion control for microrobots: An overview," *Micromachines*, vol. 6, no. 9, pp. 1346–1364, Sep. 2015.
[7] X. Zhang, H. Kim, and M. J. Kim, "Design, implementation, and analysis of a 3-D magnetic tweezer system with high magnetic field gradient," *IEEE Trans. Instrum. Meas.*, vol. 68, no. 3, pp. 680–687, Mar. 2019.

[8] J. Giltinan and M. Sitti, "Simultaneous six-degree-of-freedom control of a single-body magnetic microrobot," *IEEE Robot. Autom. Lett.*, vol. 4, no. 2, pp. 508–514, Apr. 2019.

[9] D. Li, F. Niu, J. Li, X. Li, and D. Sun, "Gradient-enhanced electromagnetic actuation system with a new core shape design for microrobot manipulation," *IEEE Trans. Ind. Electron.*, vol. 67, no. 6, pp. 4700–4710, Jun. 2020.

[10] H. Nourmohammadi, J. Keighobadi, and M. Bahrami, "Design, dynamic modelling and control of a bio-inspired helical swimming microrobot with three-dimensional manoeuvring," *Trans. Inst. Meas. Control*, vol. 39, no. 7, pp. 1037–1046, Jul. 2017.

[11] B. Chaluvadi, K. M. Stewart, A. J. Sperry, H. C. Fu, and J. J. Abbott, "Kinematic model of a magnetic-microrobot swarm in a rotating magnetic dipole field," *IEEE Robot. Autom. Lett.*, vol. 5, no. 2, pp. 2419–2426, Apr. 2020.

[12] J. Begey *et al.*, "A manipulability criterion for magnetic actuation of miniature swimmers with flexible flagellum," *IEEE Robot. Autom. Lett.*, vol. 5, no. 3, pp. 4891–4898, Jul. 2020.

[13] Y.-H. Li, C.-Y. Yen, and M.-C. Lo, "Flexibility of micromagnetic flagella in the presence of an oscillating field," *IEEE Trans. Magn.*, vol. 54, no. 11, pp. 1–5, Nov. 2018.

[14] J. K. Hamilton, P. G. Petrov, C. P. Winlove, A. D. Gilbert, M. T. Bryan, and F. Y. Ogrin, "Magnetically controlled ferromagnetic swimmers," *Sci. Rep.*, vol. 7, no. 1, Mar. 2017.

[15] V. H. Le *et al.*, "A soft-magnet-based drug-delivery module for active locomotive intestinal capsule endoscopy using an electromagnetic actuation system," *Sens. Actuators A, Phys.*, vol. 243, pp. 81–89, Jun. 2016.

[16] S. Jeon, G. Jang, H. Choi, and S. Park, "Magnetic navigation system with gradient and uniform saddle coils for the wireless manipulation of micro-robots in human blood vessels," *IEEE Trans. Magn.*, vol. 46, no. 6, pp. 1943–1946, Jun. 2010.

[17] T. Xu, G. Hwang, N. Andreff, and S. Regnier, "Planar path following of 3-D steering scaled-up helical microswimmers," *IEEE Trans. Robot.*, vol. 31, no. 1, pp. 117–127, Feb. 2015.

[18] X. Wang *et al.*, "A three-dimensional magnetic tweezer system for intraembryonic navigation and measurement," *IEEE Trans. Robot.*, vol. 34, no. 1, pp. 240–247, Feb. 2018.

[19] L. Wang, H. Xu, W. Zhai, B. Huang, and W. Rong, "Design and characterization of magnetically actuated helical swimmers at submillimeter-scale," *J. Bionic Eng.*, vol. 14, no. 1, pp. 26–33, Mar. 2017.

[20] I. S. M. Khalil, M. P. Pichel, L. Abelmann, and S. Misra, "Closed-loop control of magnetotactic bacteria," *Int. J. Robot. Res.*, vol. 32, no. 6, pp. 637–649, May 2013.

[21] B. Jang, J. Nam, W. Lee, and G. Jang, "A crawling magnetic robot actuated and steered via oscillatory rotating external magnetic fields in tubular environments," *IEEE/ASME Trans. Mechatronics*, vol. 22, no. 3, pp. 1465–1472, Jun. 2017.

[22] L. Yang, E. Yu, C.-I. Vong, and L. Zhang, "Discrete-time optimal control of electromagnetic coil systems for generation of dynamic magnetic fields with high accuracy," *IEEE/ASME Trans. Mechatronics*, vol. 24, no. 3, pp. 1208–1219, Jun. 2019.

[23] A. Mohammadi *et al.*, "Modeling and control of local electromagnetic actuation for robotic-assisted surgical devices," *IEEE/ASME Trans. Mechatronics*, vol. 22, no. 6, pp. 2449–2460, Dec. 2017.

[24] J. Lee and J.-I. Ha, "Direction priority control method for magnetic manipulation system in current and voltage limits," *IEEE Trans. Ind. Electron.*, vol. 64, no. 4, pp. 2914–2923, Apr. 2017.

[25] J. Han, "From PID to active disturbance rejection control," *IEEE Trans. Ind. Electron.*, vol. 56, no. 3, pp. 900–906, Mar. 2009.

[26] J. Kim, C. Park, J. Yoo, and S.-J. Kim, "Two-dimensional motion control of micro-robot by using two pairs of Helmholtz coils," in *Proc. IEEE Int. Symp. Robot. (ISR)*, Oct. 2013, pp. 1–2.

[27] M. P. Kummer, J. J. Abbott, B. E. Kratochvil, R. Borer, A. Sengul, and B. J. Nelson, "OctoMag: An electromagnetic system for 5-DOF wireless micromanipulation," *IEEE Trans. Robot.*, vol. 26, no. 6, pp. 1006–1017, Dec. 2010.

[28] B. L. G. Costa, V. D. Bacon, S. A. O. da Silva, and B. A. Angelico, "Tuning of a PI-MR controller based on differential evolution metaheuristic applied to the current control loop of a shunt-APF," *IEEE Trans. Ind. Electron.*, vol. 64, no. 6, pp. 4751–4761, Jun. 2017.

[29] L. Wang, M. Wang, B. Guo, Z. Wang, D. Wang, and Y. Li, "A loading control strategy for electric load simulators based on proportional resonant control," *IEEE Trans. Ind. Electron.*, vol. 65, no. 6, pp. 4608–4618, Jun. 2018.

[30] Z. Wang, C. Hu, Y. Zhu, S. He, K. Yang, and M. Zhang, "Neural network learning adaptive robust control of an industrial linear motor-driven stage with disturbance rejection ability," *IEEE Trans. Ind. Informat.*, vol. 13, no. 5, pp. 2172–2183, Oct. 2017.